Our Recent Strain-Measurement-Based Shear Modulus Reconstruction

Chikayoshi Sumi
Department of Electrical and Electronics Engineering, Faculty of Science and Technology
Sophia University Tokyo 102-8554 Japan
c-sumi@sophia.ac.jp

***Abstract*— As a differential diagnosis technique of living soft tissues, we are developing ultrasonic strain measurement-based shear modulus reconstruction methods. In this report, to stabilize the 3D and 2D reconstruction of shear modulus, Poisson's ratio and density, we propose to deal with the mean normal stress as unknown. Moreover, we propose two new methods for measuring multidimensional displacement vector with high accuracy, i.e., the multidimensional autocorrelation method and the multidimensional Doppler method. Respective displacement vector measurement methods are combined with our previously developed useful lateral modulation method, i.e., the lateral Gaussian envelope cosine modulation method (LGECMM). Effectiveness of these methods are verified by simulations and phantom experiments. Our previously developed real-time 1D reconstruction method is also reviewed and in vivo results are also presented.**

Keywords-Shear modulus, reconstruction, differential-type inverse problem, strain tensor, displacement vector, measurement, multidimensional autocorrelation method, multidimensional Doppler method, multidimensional cross-spectrum phase gradient method, regularization

I. INTRODUCTION

As a differential diagnosis technique of living soft tissues (breast, and liver, etc.), we are developing ultrasonic strain measurement-based 3D, 2D and 1D shear modulus reconstruction methods [1]. The shear modulus distribution μ is reconstructed by solving PDEs (equilibrium equations) using the reference shear moduli (i.e., initial-value problem). Recently, we have also verified the usefulness as decision tool of effectiveness of various treatments (chemotherapy, cryotherapy, thermal therapy) [1]. Meanwhile, we reported a reconstruction method utilizing a typical Poisson's ratio. However, as reconstruction errors were confirmed due to the difference between the original value and the set value of the Poisson's ratio [1], we proposed a method to reconstruct the Poisson's ratio as well by dealing with the Lame's constants λ and μ as unknown [2]. Furthermore, we proposed to reconstruct the density as well to allow dealing with dynamic deformation (i.e., motion equations) [2].

In this report, to stabilize the reconstruction of these mechanical properties even when the target tissue is incompressible, we propose to use the mean normal stress as unknown instead of λ [3]. As we utilize our previously developed regularized implicit-integration approach using the iterative method (conjugate gradient method) to solve the PDEs, when neither Poisson's ratio nor mean normal stress is target, their references are needless (reconstructions of the Poisson's ratio and the mean normal stress become dependent on respective initial estimates of the iterative method). Thus, this method is also useful when neither reference Poisson's ratio nor reference mean normal stress can be set.

Realizing high accuracy in measuring tissue strain tensor can be achieved by the use of a lateral modulation method [4] and a displacement vector measurement method that provides simultaneous axial and lateral measurements, e.g., our previously developed cross-spectrum phase gradient method (CSPGM) [5,6]. In this report, two new methods are also described for such simultaneous measurements using an instantaneous ultrasound signal phase, i.e., the multidimensional autocorrelation method and the multidimensional Doppler method [7-9]. High measurement accuracy is achieved by combining respective methods with our developed lateral Gaussian envelop cosine modulation method (LGECMM) [8,9]. These methods can also be used for measurements of blood flow, sonar data and other target motion.

Shear modulus reconstruction obtained by the new shear modulus reconstruction method and the new displacement measurement method is shown for an agar phantom.

Finally, we review our developed real-time 1D reconstruction methods [5,10,11]. Since the 2D and 3D reconstruction require a special US data acquisition system to accurately measure the strain tensor field, 1D reconstruction utilizing standard US imaging equipment is considered to be still clinically useful. When the axial strain can be measured with high accuracy, for 1D reconstruction, the calculated ratio of the strains generated in the direction of predominant deformation along the direction can be used as the final estimate of the target's shear modulus at a normal position where no singularity occurs (change of the sign of strain or numerically infinitesimal absolute strain sometimes occurs at stiff region) [1], and then 1D implicit-integration is performed only at the singular positions (i.e., partial implicit-integration) which substantially reduces computation time. The shear modulus distribution resulting from calculated ratio of the measured strains is also utilized as an initial estimate in 1D, 2D, and 3D implicit-integration (when measured strain is inaccurate, reconstruction should be sufficiently regularized with utilization of a uniform initial estimate as performed for monitoring of thermal treatment) [1].

II. MULTI-DIMENSIONAL SHEAR MODULUS RECONSTRUCTION

A. Method

As living soft tissues deform in 3D space due to arbitrary mechanical sources, multidimensional signal processing [5-9] realizes high accuracy deformation measurement (acceleration vector and strain tensor) and mechanical properties reconstruction.

By measuring the acceleration vector α_i (i = 1-3) and the strain tensor ε_{ij} (i,j = 1-3) throughout the 3D ROI (region of interest), motion equations are dealt with as the simultaneous first order partial differential equations (PDEs) for unknown distributions of the Lame's constants λ, μ and the density ρ, i.e.,

$$\rho\alpha_i = \{\varepsilon_{\alpha\alpha}\delta_{ij}\}\lambda_{,j} + \{\varepsilon_{\alpha\alpha}\delta_{ij}\}_{,j}\lambda + 2\varepsilon_{ij}\mu_{,j} + 2\varepsilon_{ij,j}\mu,$$

$$\text{where } \lambda = \frac{2\nu}{1-2\nu}\mu, \mu : \text{shear modulus}, \nu : \text{Poisson's ratio.}$$

Provided that the references of the Lame's constants or density are given in the ROI, this reconstruction problem becomes an initial-value problem for the unknown distributions [2].

In this report, by dealing with the mean normal stress p (product of λ and $\varepsilon_{\alpha\alpha}$) as unknown, we stabilize shear modulus reconstruction [3]. To reconstruct the distribution of the shear modulus, Poisson's ratio (or mean normal stress) and density, the following reference (initial) values must be given in the ROI, i.e., the references of Poisson's ratio (or mean normal stress) and either shear modulus or density. When neither Poisson's ratio nor mean normal stress is target, their references are needless. In this case, as we utilize the iterative method to solve this problem, reconstruction of the mean normal stress is dependent on the initial estimate of the iterative method. We utilize the conjugate gradient method.

When dealing with the static equilibrium case, only the shear modulus and the Poisson's ratio (or mean normal stress) are targets.

In order to uniquely obtain the stable reconstructions, proper configurations of mechanical sources and reference regions should be realized such that the reference regions widely extend in directions crossing the predominant tissue deformation [12].

In order to further stabilize reconstruction, regularization [1,13] is respectively applied to the shear modulus, mean normal stress and density using different regularization parameters.

On 2D reconstruction, when the number of the unknown distribution is larger than 2, independent deformation fields must be measured.

B. Simulation

First, reconstruction of the shear modulus and Poisson's ratio is shown by dealing with a static equilibrium case [3]. A simulated inhomogeneous cubic phantom (50.0 mm sides) was uniformly compressed in the axial direction (x-axis) with a displacement of 0.25 mm. The phantom includes a spherical inclusion at a depth x = 25.0 mm (5-mm radius) having twice as high a shear modulus as that of the surrounding medium, i.e., 2.0×10^5 N/m^2 versus 1.0×10^5 N/m^2. The Poisson's ratio of the inclusion is 0.4, while the value of the surrounding medium is 0.47 (Phantom 1). The resultant internal displacement vector field was calculated by the successive over relaxation (SOR) method. A cubic ROI (30.0 mm sides) is set at the center of the phantom, which has the spherical inclusion at the central part. The reference region is set (30.0 mm $\times$ 30.0 mm) at the upper surface of the ROI.

Figure 1 shows 3D reconstruction, and both 2D reconstructions respectively obtained under the assumptions of 2D strain and 2D stress conditions. We considered the following three cases (i)-(iii), i.e., the mean normal stress is dealt with as unknown (i) with the reference (initial) values and (ii) without the reference values, and (iii) λ is dealt with as unknown.

Figure 1 shows 3D reconstructions with elevational position z = 25.0 mm of shear modulus and Poisson's ratio (2D reconstructions obtained under assumptions of 2D strain and 2D stress are omitted). Although 3D and 2D reconstructions were unstable when dealing with λ as unknown, the reconstructions became stable by dealing with the mean normal stress as unknown. Figure 2a–2c respectively shows axial x-profiles, lateral y-profiles, and elevational z-profiles of the reconstructions of shear modulus and Poisson's ratio passing through the center of the spherical inclusion. Table I shows the means of the shear moduli and Poisson's ratios evaluated at the central square region of the inclusion (5.0 mm x 5.0 mm). Table II shows the

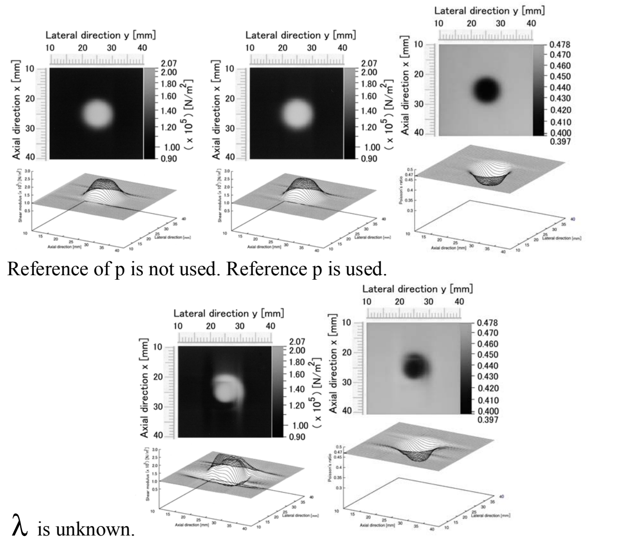

Fig. 1. 3D reconstructions of shear modulus and Poisson's ratio (Phantom 1).

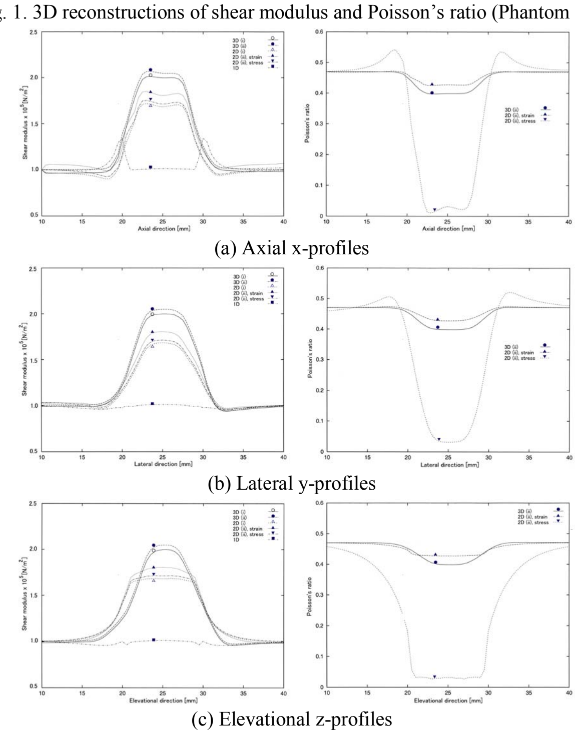

Fig. 2. 3D reconstruction, both 2D reconstructions (2D strain and 2D stress assumptions) and 1D reconstruction of shear modulus and Poisson's ratio (Phantom 1).

Table I. Reconstructions of shear modulus and Poisson's ratio (Phantom 1). Means at central square region (5.0 mm x 5.0 mm).

Dimension	Reference p	Shear modulus ($\times 10^5$) [N/m^2]	Poisson's ratio
3D	(i) Not used.	1.94	–
	(ii) Used.	1.99	0.402
2D	(i) Not used.	1.64	–
2D strain	(ii) Used.	1.76	0.429
2D stress	(ii) Used.	1.67	4.40×10^{-2}
1D	–	1.01	–

corresponding results obtained on Phantom 2 which has the Poisson's ratio of 0.47 in the inclusion and 0.40 in the surrounding medium.

Although 3D reconstruction was quantitative, both 2D reconstructions (2D strain and 2D stress assumptions) were less quantitative. Specifically, for both 2D reconstructions, the shear modulus of the stiff inclusion is estimated to be smaller than that of the original (for other phantoms, the shear modulus of the soft inclusion is estimated to be larger than that of the original, not shown). When assuming the 2D strain condition, the large Poisson's ratio of the inclusion is estimated to be smaller than that of the original, while the small value of the inclusion is estimated to be larger than that of the original. When assuming the 2D stress condition, the large Poisson's ratio of the inclusion is estimated to be much larger than that of the original, while the small value of the inclusion is estimated to be much smaller than that of the original.

For phantom 1, 1D shear modulus reconstruction (Table I) as well as axial strain imaging is useless [3,11]. That is, the inclusion could not be detected. That is, it is difficult to detect a region having high shear moduli and low Poisson's ratios and vice versa by using the axial strain image and the 1D reconstruction image.

Regarding with the spatial resolution of the reconstructions of shear modulus and Poisson's ratio, for both 2D reconstructions (2D strain and 2D stress assumptions), the size of the stiff lesion is estimated to be larger than those of both the original and 3D reconstruction (Fig. 2). 2D reconstructions are affected by inhomogeneity in neighboring planes.

These are erroneous artifacts due to the low dimensionality of reconstruction.

B. Reconstruction of shear modulus, Poisson's ratio, and density

Next, reconstruction of the shear modulus, Poisson's ratio and density is shown by dealing with a dynamic deformation case [3].

3D reconstructions were performed in four cases, i.e., reference of (i) only shear modulus, (ii) shear modulus and mean normal stress, (iii) only density and (iv) density and mean normal stress were used. The Phantom 2 was uniformly vibrated in the axial direction (x-axis) with a displacement of 0.25 mm and a frequency of 1. Hz. The density was uniformly set at 1.0 g/cm^3. The same ROI was used.

Figure 3 shows 3D reconstructions for case (ii) with elevational position z = 25.0 mm. In all cases, reconstructions were quantitatively obtained. Table III shows the means of the shear moduli, Poisson's ratios and densities evaluated at the central square region of the inclusion (5.0 mm x 5.0 mm).

III. MULTI-DIMENSIONAL DISPLACEMENT VECTOR MEASUREMENT

A. Multidimensionalautocorrelation method and multidimensional Doppler method

To realize measurement of 3D displacement vector (u_x, u_y, u_z), four or three 3D complex signals with different single octant spectra that extend analytic signal are calculated for pre- and post- rf-echo data, respectively [7-9]. The displacement vector (u_x, u_y, u_z) is obtained by solving the following simultaneous equations (four or three independent equations) derived from the complex signals. In (1) multidimensional autocorrelation method, an equation holds for the phase θ of each autocorrelation signal obtained from a paired of complex signals, i.e.,

$$\theta + \frac{\partial}{\partial x}\theta u_x + \frac{\partial}{\partial y}\theta u_y + \frac{\partial}{\partial z}\theta u_z = 0,$$

in (2) multidimensional Doppler method, an equation holds for the phase θ of each complex signal, i.e.,

$$\frac{\partial}{\partial t}\theta\Delta t + \frac{\partial}{\partial x}\theta u_x + \frac{\partial}{\partial y}\theta u_y + \frac{\partial}{\partial z}\theta u_z = 0,$$

where Δt is the pulse repetition interval. $\partial / \partial t \cdot \theta\Delta t$ can also be obtained as phase θ by evaluating each autocorrelation signal.

When measuring 2D displacement vector, two 2D complex signals with different single quadrant spectra are calculated, and correspondingly derived simultaneous equations (two independent equations) are solved.

Large displacements are dealt with by combining the CSPGM or the cross-correlation method. To improve measurement accuracy, phase matching [5] is also performed.

B. Lateral Gaussian Envolpe cosine modulation (LGECM)

This modulation method is comprised of the processes of apodization and focusing [8,9]. In Jensen's method [4], the finite width aperture must be apodized using the sinc functions.

Table II. Reconstructions of shear modulus and Poisson's ratio (Phantom 2). Means at central square region (5.0 mm x 5.0 mm).

Dimension	Reference p	Shear modulus ($\times 10^5$) [N/m^2]	Poisson's ratio
3D	(i) Not used.	2.07	–
	(ii) Used.	2.12	0.469
2D	(i) Not used.	1.66	–
2D strain	(ii) Used.	1.76	0.447
2D stress	(ii) Used.	1.70	0.679
1D	–	2.06	–

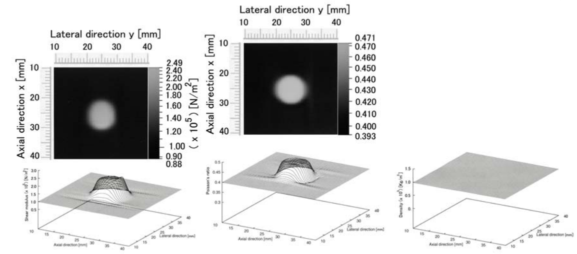

Fig. 3. 3D reconstructions (case ii) of shear modulus, Poisson's ratio, and density obtained under the condition of 3D (x,y,z) stress (Phantom 2).

Table III. Reconstructions of shear modulus, Poisson's ratio, and density (Phantom 2). Means at central square region (5.0 mm x 5.0 mm).

Dimension	Reference	Shear modulus ($\times 10^5$) [N/m^2]	Poisson's ratio	Density ($\times 10^3$) [Kg/m^3]
3D	(i) μ	2.06	–	1.00
3D	(ii) μ & p	2.12	0.469	1.00
3D	(iii) ρ	2.14	-	1.00
3D	(iv) ρ & p	2.17	0.469	1.00

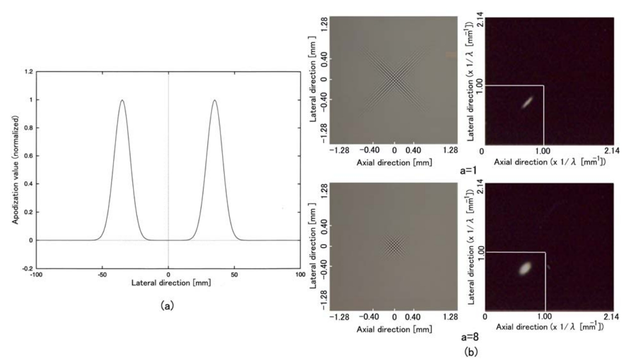

Fig. 4. Lateral Gauss envelop cosine modulation. Ultrasound speed 1,500m/s, US frequency 3.5MHz, depth 35mm, σ_y 0.4mm, f_y (1/ λ) mm^{-1}. Axial direction also Gaussian PSF with σ_x of 0.4mm. (a) Apodization value. (b) PSF and spectrum when setting a=1, and 8.

With this in mind, we realize the Gaussian type point spread function as the lateral-elevational (yz) point spread function, i.e.,

$$\exp\left(-\frac{y^2}{2\sigma_y^2}-\frac{z^2}{2\sigma_z^2}\right)\cos(2\pi f_y y)\cos(2\pi f_z z),$$

where f_y and f_z are respectively the lateral y and elevational z modulation frequencies, and σ_y and σ_z respectively correspond to the lateral y and elevational z beam widths. Based on the Fraunhofer's approximation, for apodization of the depth x, the following apodization function is utilized, i.e.,

$$\begin{aligned}\frac{1}{4\lambda x}\{&\exp[-\frac{(2\pi)^2(\frac{y}{\lambda x}+f_y+f_a)^2 a\sigma_y^2}{2}-\frac{(2\pi)^2(\frac{z}{\lambda x}+f_z+f_b)^2 b\sigma_z^2}{2}]\\ &+\exp[-\frac{(2\pi)^2(\frac{y}{\lambda x}+f_y+f_a)^2 a\sigma_y^2}{2}-\frac{(2\pi)^2(\frac{z}{\lambda x}-f_z-f_b)^2 b\sigma_z^2}{2}]\}\\ &+\exp[-\frac{(2\pi)^2(\frac{y}{\lambda x}-f_y-f_a)^2 a\sigma_y^2}{2}-\frac{(2\pi)^2(\frac{z}{\lambda x}+f_z+f_b)^2 b\sigma_z^2}{2}]\\ &+\exp[-\frac{(2\pi)^2(\frac{y}{\lambda x}-f_y-f_a)^2 a\sigma_y^2}{2}-\frac{(2\pi)^2(\frac{z}{\lambda x}-f_z-f_b)^2 b\sigma_z^2}{2}]\},\end{aligned}$$

where λ is the ultrasound wavelength, f_a and f_b are respectively parameters introduced to regulate the lateral y and elevational z modulation frequencies, and a and b are respectively parameters introduced to regulate the lateral y and elevational z bandwidths.

In Fig. 4a, the apodization function only for lateral y modulation is shown, where at depth x = 35. mm, f_y and σ_y are respectively set to $(1/\lambda)$ mm^{-1} and 0.4 mm when the ultrasound velocity and the ultrasound frequency are respectively 1,500 m/s and 3.5 MHz. Simply, here, the point spread function and the spectrum are shown when transmitting plane waves (Fig. 4b, a = 1 and 8). The axial point spread function is realized using the Gaussian type point spread function (standard deviation, 0.4 mm). As shown, the bandwidth became narrower than the designed bandwidth (a = 1.). It is needless to say that the inappropriateness of the approximation causes the difference. The difference might be compensated by using the parameter a (a = 8.). In addition, the lateral modulation might also be compensated by using f_a. However, our developed multidimensional autocorrelation method and multidimensional Doppler method estimate the ultrasound frequency and lateral modulation frequency and these methods do not use bandwidths. Furthermore, the CSPGM [5,6] do not needs these values. In addition, all these methods are robust to the frequency modulations due to scattering and attenuation.

C. Simulations

Here, simply, 2D displacement vector measurements were simulated [8,9]. The distributions of displacement vector (0.01 mm, 0.01 mm) were evaluated. Pre- and post- 2D echo data were simulated by convolving the 2D Gaussian type point spread function (σ_x = σ_y = 0.4mm) with white data. The measurement accuracy (SNR) was evaluated by changing the lateral modulation frequency and beam width (σ_y) when setting the ultrasound frequency at 3.5 MHz. The ultrasound speed was set at 1,500 mm/s, and sampling frequency was set at 15. MHz, and the beam pitch was set at 0.05 mm. White noises were added to the pre- and post- echo data. The results were shown when the echo's SNRs were 20 dB and ∞ dB (no noise).

Figure 5 shows the SNRs versus the lateral modulation wavelength obtained when setting the spatial moving average width

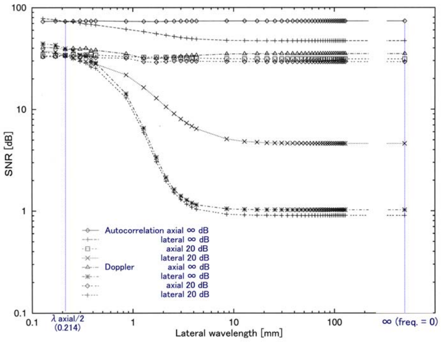

Fig. 5. Lateral wavelength versus SNRs of axial and lateral displacements measured using multidimensional autocorrelation method and multidimensional Doppler method (echo data SNRs ∞ dB and 20 dB). Moving average width 64×64.

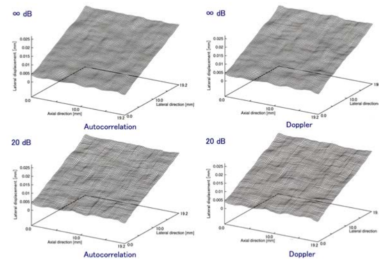

Fig. 6. Lateral displacement measurement results using multidimensional autocorrelation method and multidimensional Doppler method (echo data SNRs dB and 20 dB). Moving average width 64×64.

at 64×64 points (3.2 mm $\times$ 3.2 mm) for calculating the phase and the spatial derivatives. Here, we should keep in mind that the phase of the autocorrelation signal evaluated from the spatio-temporal moving-averaged real and imaginary components yields accurate displacement vector measurement than the spatio-temporal moving-averaged phase (results omitted) [7]. For the autocorrelation method the spatial derivatives of the autocorrelation signal phase can be obtained from the phases by finite-difference approximation or differentiation using differential filters with cutoff frequencies, while for the Doppler method the spatial and temporal derivatives of the complex signal phase can be obtained by spatio-temporal moving-averaging the derivatives of the raw phase or by differentiating the spatio-temporal moving-averaged phase (finite-difference approximation or differential filter is used). Here spatial moving-averaging was performed and the finite difference was employed. The phase $\partial/\partial t \cdot \theta \Delta t$ was obtained from autocorrelation signal. The measurement accuracy of the axial displacement was sufficiently high regardless the lateral modulation frequency. When SNR is 20dB, both methods yield higher SNRs than 30 dB. However, the accuracy of the lateral displacement degrades compared to that of the axial displacement when the lateral modulation wavelength is longer than the half of the ultrasound wavelength. The accuracy of the multidimensional autocorrelation method was higher than the multidimensional Doppler method, whose calculation amount is less than that of the autocorrelation method. When not laterally modulating the echo, if the echo data is noiseless, the measurement accuracy of the lateral displacement was sufficiently high (higher than 40 dB). However, the accuracy considerably degrades when the echo's SNR becomes low. The results obtained when setting the moving average width at 32×32 (1.6 mm $\times$ 1.6 mm), 16×16, 8×8 points are omitted. The moving average width being set smaller, all the measurement accuracy degrades. Particularly, it was remarkable for the multidimensional autocorrelation method at long lateral wavelength. Specifically, the accuracy of the lateral displacement becomes lower at 32×32 (20dB) than the multidimensional Doppler's method, and the accuracy of axial displacement becomes lower at 16×16 (20 dB) than the multidimensional Doppler's method. At 8×8, both the accuracy becomes lower at all the lateral wavelength. These two methods allow more accurate measurement than the CSPGM using a window having the same size as that of moving average (results omitted). Moreover, these methods realize less calculation amount than the CSPGM. When setting the respective lateral modulation frequency and σ_x at $(2/\lambda)$ mm^{-1} and 0.4 mm, and changing σ_y from 0.4 mm to larger value (6.4 mm) under a constant SNR of echo data, the accuracy of the axial and lateral displacement measurements slightly degrade (results omitted).

Next, 2D displacement vector measurements were simulated when stain exists, i.e., the axial and lateral strains of 0.12 percent. The ultrasound frequency was 3.5 MHz, and the lateral modulation frequency was $(2/\lambda)$ mm^{-1}. White noises were added to the echo data. Figure 6 shows for the moving-average width of 64×64 the measured lateral displacement distributions when echo's SNR were ∞ dB and 20 dB (32×32, 16×16; 8×8, omitted). When setting the moving average width small, the measurement became unstable and the measurement accuracy degrades.

To realize high measurement accuracy, the lateral modulation frequency and ultrasound frequency should be set higher if echo SNR is same. Moreover, the beam width and pulse length should be set narrower and shorter, respectively. These conditions yield high spatial resolution measurement as well. Utilization of the large moving average width stabilizes measurement at trade off with spatial resolution. However, phase matching [5,6] and echo compression/stretching allows heightening the spatial resolution as well as the measurement accuracy.

IV. PHANTOM EXPERIMENTS

Phantom experiments were performed. The target agar-graphite phantom has a stiff cylindrical inclusion (dia., 10 mm, 2.95×10^6 N/m^2 vs. 1.43×10^6 N/m^2). Fig. 7a and 7b respectively shows the axial and lateral strain images (ROI, 12.6 mm x 14.2 mm) measured by the 2D autocorrelation method. We previously confirmed that the regularization method was effective to stabilize the displacement vector measurement when using the CSPGM [13]. Briefly, the effectiveness of the regularization was also verified for the multidimensional autocorrelation method. Fig. 7c shows a stable lateral strain image obtained when regularizing only lateral displacement (L_2-norm of Laplacian was used as a penalty term). Simultaneously obtained axial strain image is similar with Fig. 7a. In contrast, Fig. 7d shows a low-pass filtered lateral strain image of Fig. 7b. Fig. 7e shows the regularized shear modulus reconstruction image obtained using the regularized strains. The shear modulus of the stiff inclusion was estimated to be 1.71×10^6 N/m^2. Due to low dimensionality of reconstruction, non-modulation and regularization, the shear modulus was estimated to be lower to the original value though the stable reconstruction was obtained.

IV. REAL-TIME SHEAR MODULUS RECONSTRUCTION

Other erroneous artifacts for 1D reconstruction were found for other phantoms (having uniform Poisson's ratio and a stiff or soft inclusion) are described in [1]. Summarizing the artifacts, i.e., (1) Quantitativeness is degraded, i.e., the stiff region and the stress

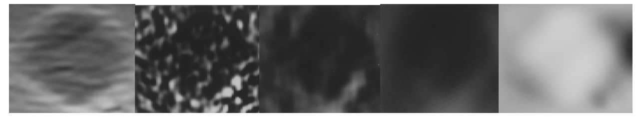

(a) (b) (c) (d) (e)

Fig. 7. Agar phantom experiments (ROI, 12.6 mm $\times$ 14.2 mm). (a) Axial strain image, (b) lateral strain image (nonregularized), (c) regularized lateral strain image, (d) low-pass filtered lateral strain image and (e) regularized shear modulus reconstruction image. Axial strain image ranges from -1.6×10^{-2} to 0. Lateral strain image ranges from 0 to 1.6×10^{-2}. Shear modulus image ranges from 0.70×10^6 N/m^2 to 1.71×10^6 N/m^2.

concentration in front of and behind the stiff region is estimated to be softer, while the soft region and the stress weak region in front of and behind the soft region is estimated to be stiffer. (2) The lateral and elevational sizes are estimated to be larger than the original sizes.

A 59-year-old female volunteer with a scirrhous carcinoma was supinely positioned [10]. To obtain absolute shear modulus reconstruction, an agar phantom with a shear modulus of 1.4×10^6 N/m^2 was used as reference (a block of 40 mm (axial) $\times$ 80 mm $\times$ 80 mm). Although the block of reference should be thinner, the occurrence of multiple reflection using an agar phantom prevents us from utilizing a thin block. Fig. 8a shows a B-mode image of an ROI of 29.0 mm $\times$ 44.6 mm at a depth of 36.1 mm from the transducer (skin surface). The reference line was set at the upper borderline of the ROI (depth, 36.1 mm) existing in the agar phantom. During compression, rf echo data frames were successively acquired. The interrogating ultrasound had a US nominal frequency f_c of 7.5 MHz and was sampled at a rate f_s of 30 MHz in 12 bits. An axial strain image is shown in Fig. 8b in a linear gray scale obtained using the CSPGM [5,6] (local region size, 0.8 mm $\times$ 3.8 mm) and a differential filter with a cutoff frequency of 0.82 mm^{-1}.

Figures 9a and 9b respectively show reconstruction images of the shear modulus and the inverse of the shear modulus obtained by calculating the ratio of strains. In these images, the structures of the scirrhous carcinoma and the surrounding normal tissues are quantitatively visualized, although the erroneous artifacts might be present in that the shear modulus image could have variations in neighboring planes. The carcinoma was estimated to have considerably high shear moduli. Where singular regions occurred (i.e., stiff regions), they were respectively given an upper bound and a lower bound determined by a relative shear modulus (= 10.0). These images are confirmed to be laterally unstable (e.g., arrows at a lateral position of 22.5 mm in Figs. 9a and 9b). Figures 9c and 9d respectively show low-pass-filtered reconstructions of the shear modulus (9a) and the inverse of the shear modulus (9b). By low-pass filtering, the reconstructions become laterally stable. However, the spatial resolution of the low-pass-filtered reconstruction of the shear modulus becomes substantially low. Empirically, low-pass filtering should be applied to the inverse of the shear modulus. Figures 10a and 10b respectively show profiles of the low-pass-filtered reconstructions of the shear modulus and the inverse of the shear modulus at a lateral position of 22.5 mm. Figure 9e shows the shear modulus reconstruction obtained by inverting the low-pass-filtered reconstruction of the inverse of shear modulus (9d).

Next, the stably obtained reconstructions of the shear modulus and the inverse of the shear modulus are shown in Figs. 9f and 9g using strains with a low spatial resolution in the reference region. Here, the strains are moving-averaged though they can also be low-pass filtered. Both reconstructions of the shear modulus and the inverse of the shear modulus are evaluated at high spatial resolutions. Although the stably obtained reconstructions of the shear modulus

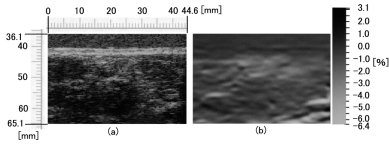

Fig. 8. *In vivo* human breast scirrhous carcinoma tissue. A block of reference material (thickness: 40 mm) of known shear modulus (= 1.4 × 10^6 N/m^2) was placed between the ultrasound transducer and the patient's breast. The ROI (29.0 mm × 44.6 mm) was set at a depth of 36.1 mm. (a) B-mode image and (b) strain image.

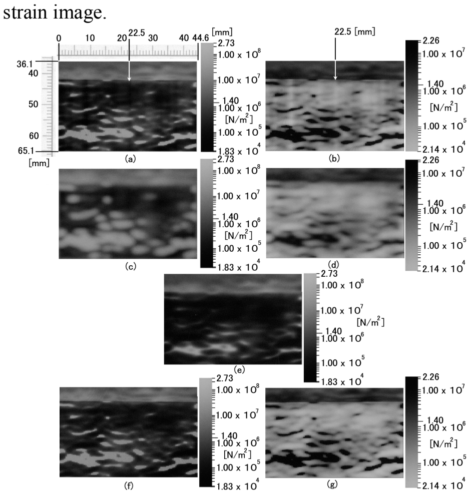

Fig. 9. 1D shear modulus reconstructions obtained by calculating strain ratio. References are taken at points on the line of 36.1 mm depth (reference line). (a) Shear modulus. (b) Inverse of shear modulus. (c) Low-pass-filtered (a). (d) Low-pass-filtered (b). (e) Inverse of (d). (f) Shear modulus obtained using moving-averaged strains at the reference line. (g) Inverse of shear modulus obtained using moving-averaged strains at the reference line.

(a) 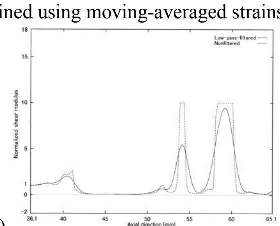 (b) 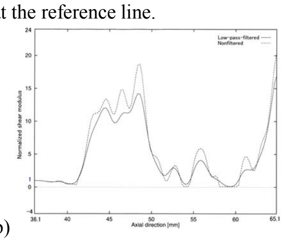

Fig. 10. Low-pass-filtered and nonfiltered reconstruction profiles at lateral position of 22.5 mm of (a) shear modulus and (b) inverse of shear modulus.

(9f) and the inverse of the shear modulus (9g) are evaluated at high spatial resolutions respectively compared to reconstructions (9c) and (9d), they are possibly less quantitative if the reference region is set at stress concentration [10]. Then, implicit integration should be performed using the reconstruction (9f) and (9g) as the initial distributions (shown in [10]). The quantitativeness of reconstruction is significantly improved.

Summarizing, the calculation of strain ratio and the imaging is useful when the strain is accurately measured. Low-pass filtering should be applied to the inverse of the shear modulus distribution. Evaluation of strain with low spatial resolution at reference regions is effective except when the reference is set in stress concentration regions and stress weak regions in front of and behind stiff and soft regions. Implicit-integration yields an acceptable, stable reconstruction by utilizing *a priori* knowledge. Partial implicit-integrations is also useful when the measured strain is accurate. Thus, the shear modulus value can be obtained throughout a ROI from the reconstruction image obtained in real-time of which erroneous artifacts are reduced and singularity is treated.

V. Conclusions

In this report, we proposed a new shear modulus reconstruction method using the mean normal stress as unknown. We showed through simulations that this reconstruction method yields stable reconstructions of the shear modulus, Poisson's ratio and density. It is considered that it is difficult to set the reference values of the mean normal stress and the Poisson's ratio. This reconstruction method is also useful in these cases. Furthermore, we proposed new two displacement vector measurement methods, i.e., the multidimensional autocorrelation method and the multidimensional Doppler method. Furthermore, their measurement accuracies were evaluated through simulations. Feasibility of the combined multidimensional strain-measurement-based shear modulus reconstruction was confirmed through phantom experiments. The effectiveness of the regularization method will be more specifically evaluated together with the methods for setting the regularization parameters [13-15].

Real-time 1D reconstruction methods were also reviewed.

References

[1] C. Sumi, "Usefulness of ultrasonic strain measurement-based shear modulus reconstruction for diagnosis and thermal treatment," *IEEE Trans. on UFFC*, October 2005 (in press).

[2] C. Sumi, "Usefulness of ultrasonic strain-measurement-based mechanical properties imaging technique – Toward realization of combined short time diagnosis/treatment," *Proc. of 18th Int. Congress on Acoustics Kyoto*, II 901-904, April 2004.

[3] C. Sumi, "Reconstruction of shear modulus distribution together with Poisson's ratio distribution and density distribution," *Proc. of 27th Int. Conf. of IEEE EMBS*, CD-ROM, September 2005.

[4] J. A. Jensen "A new method for estimation of velocity vectors," *IEEE Trans. on UFFC*, vol. 45, pp. 837-851, 1998.

[5] C. Sumi etal., "Phantom experiment on estimation of shear modulus distribution in soft tissue from ultrasonic measurement of displacement vector field," *IEICE Trans. on Fundamental*, vol. E78-A, no. 12, pp. 1655-1664, December 1995.

[6] C. Sumi etal, "Fine elasticity imaging on utilizing the iterative rf-echo phase matching method," *IEEE Trans. on UFFC*, vol. 46, no. 1, pp. 158-166, January 1999.

[7] C. Sumi, "Digital measurement method of tissue displacement vector from instantaneous phase of ultrasonic echo signal," *Technical report of Japn. Soc. of Ultrason. in Med.*, vol. 102, no. 4, pp. 37-40, December 2002.

[8] C. Sumi, "Accuracy evaluation of multidimensional displacement vector measurement methods utilizing instantaneous phase – Multidimensional autocorrelation method and multidimensional Doppler method," *Technical report of IEICE*, US2004-104, pp. 13-18, March 2005.

[9] C. Sumi, "Multidimensional displacement vector measurement methods utilizing instantaneous phase," *Proc. of 27th Int. Conf. of IEEE EMBS*, CD-ROM, September 2005.

[10] C. Sumi etal, "An effective ultrasonic strain-measurement-based shear modulus reconstruction technique for superficial tissues --- demonstration on *in vitro* pork ribs and *in vivo* human breast tissues," *Physics in Medicine and Biology*, vol. 45, pp. 1511-1520, June 2000.

[11] C. Sumi, "Real-time reconstruction of shear modulus distribution by calculating strain ratio," *Proc. of 27th Int. Conf. of IEEE EMBS*, CD-ROM, September 2005.

[12] C. Sumi etal, "A robust numerical solution to reconstruct a globally relative shear modulus distribution from strain measurements," *IEEE Trans. on MI*, vol. 17, pp. 419-428, June 1998.

[13] C. Sumi and T. Yamada, "Stabilization of tissue displacement vector measurement utilizing ultrasonic cross-spectrum," *Technical report of Japn. Soc. of Ultrason. in Med.*, vol. 101, no. 4, pp. 31-41, December 2001.

[14] C. Sumi, "Simulation study of reconstruction of shear modulus, density, Poisson's ratio distributions (2nd report)," *4th Int. Conf. Ultrason. Meas. and Imag. of Tissue Elasticity*, October 2005.

[15] C. Sumi, "Regularization for strain measurement and shear modulus reconstruction," *4th Int. Conf. Ultrason. Meas. and imag. of Tissue Elasticity*, October 2005.